Magnetic Resonance Imaging 34 (2016) 940–950

Contents lists available at ScienceDirect

Magnetic Resonance Imaging

journal homepage: www.mrijournal.com

Original contribution

GOCART: GOlden-angle CArtesian randomized time-resolved 3D MRI

Yinghua Zhu [a,*], Yi Guo [a], Sajan Goud Lingala [a], R. Marc Lebel [b,c], Meng Law [d], Krishna S. Nayak [a]

[a] Ming Hsieh Department of Electrical Engineering, Viterbi School of Engineering, University of Southern California, Los Angeles, USA
[b] Applied Science Laboratory, GE Healthcare, AB, Calgary, Canada
[c] Foothills Medical Center, Calgary, Canada
[d] Department of Radiology, Keck School of Medicine, University of Southern California Medical Center, Los Angeles, USA

ARTICLE INFO

Article history:
Received 20 July 2015
Revised 15 December 2015
Accepted 16 December 2015

Keywords:
DCE
Time resolved 3D MRI
Dynamic golden angle
Randomized sampling
Constrained reconstruction

ABSTRACT

Purpose: To develop and evaluate a novel 3D Cartesian sampling scheme which is well suited for time-resolved 3D MRI using parallel imaging and compressed sensing.
Methods: The proposed sampling scheme, termed GOlden-angle CArtesian Randomized Time-resolved (GOCART) 3D MRI, is based on golden angle (GA) Cartesian sampling, with random sampling of the k_y-k_z phase encode locations along each Cartesian radial spoke. This method was evaluated in conjunction with constrained reconstruction of retrospectively and prospectively undersampled in-vivo dynamic contrast enhanced (DCE) MRI data and simulated phantom data.
Results: In in-vivo retrospective studies and phantom simulations, images reconstructed from phase encodes defined by GOCART were equal to or superior to those with Poisson disc or GA sampling schemes. Typical GOCART sampling tables were generated in <100 ms. GOCART has also been successfully utilized prospectively to produce clinically valuable whole-brain DCE-MRI images.
Conclusion: GOCART is a practical and efficient sampling scheme for time-resolved 3D MRI. It shows great potential for highly accelerated DCE-MRI and is well suited to modern reconstruction methods such as parallel imaging and compressed sensing.

Introduction

Time-resolved 3D MRI is an imaging technique that enables contrast-enhanced MR angiography (CE-MRA) and dynamic contrast enhanced (DCE) MRI. CE-MRA and DCE-MRI are both dynamic and utilize the same enhancement mechanism, but they have different goals. CE-MRA focuses on vascular signal, where contrast agent concentrations are very high, and high spatiotemporal resolution is critical. DCE-MRI, however, focuses on tissue signals, where contrast agent concentrations are lower, change more slowly, and these subtle changes allow one to quantify pharmacokinetics.

Various sampling and reconstruction techniques have been proposed to address and improve the spatial versus temporal resolution trade-off in CE-MRA and DCE-MRI. Early view-sharing methods such as keyhole [1] and time-resolved imaging of contrast kinetics (TRICKS) [2] filled the missing data from adjacent time frames. Since non-Cartesian sampling is more robust to motion and efficient for dynamic imaging, TRICKS was extended to use radial projections [3] and spirals [4]. Other non-Cartesian implementations include k-space weighted image contrast (KWIC) [5], golden angle stack-of-stars [6], vastly undersampled isotropic projection reconstruction (VIPR) [7], highly constrained back projection (HYPR) [8], and stack-of-spirals [9].

Non-Cartesian sequences are often limited by gradient errors and off-resonance artifacts. For this reason, many investigators have reverted to Cartesian sequences where the phase encode (PE) order provides variable density much like non-Cartesian approaches. Such sequences include Cartesian projection reconstruction (CAPR) [10], stochastic trajectories (TWIST) [11], interleaved variable density (IVD) [12], a multi-level radial profile ordering [13], differential subsampling with Cartesian ordering (DISCO) [14], variable-density Poisson ellipsoid [15] and an ordering that gradually improves spatial resolution [16].

Cartesian and non-Cartesian sequences have also been combined, starting with time resolved interleaved projection sampling with 3D Cartesian Phase and Slice encoding (TRIPPS) [17], which applied rasterized radials on the PE plane, and golden angle radial phase encoding (Golden-RPE) [18], which combined radial sampling and Cartesian readouts. TRIPPS and Golden-RPE were succeeded by golden angle (GA) variants [19], variable-density radial (VDRad) [20] and golden angle spiral variants [21].

Most of the aforementioned methods accelerate time-resolved MRI by undersampling in k-space, and used parallel imaging [22,23] and/or compressed sensing [24] for reconstruction. Poission disc

* Corresponding author at: 3740 McClintock Avenue, EEB Room 400, Los Angeles, CA 90089-2564. Tel.: +1 213 821 4110; fax: +1 213 740 4651.
E-mail address: yinghuaz@usc.edu (Y. Zhu).

http://dx.doi.org/10.1016/j.mri.2015.12.030
0730-725X/

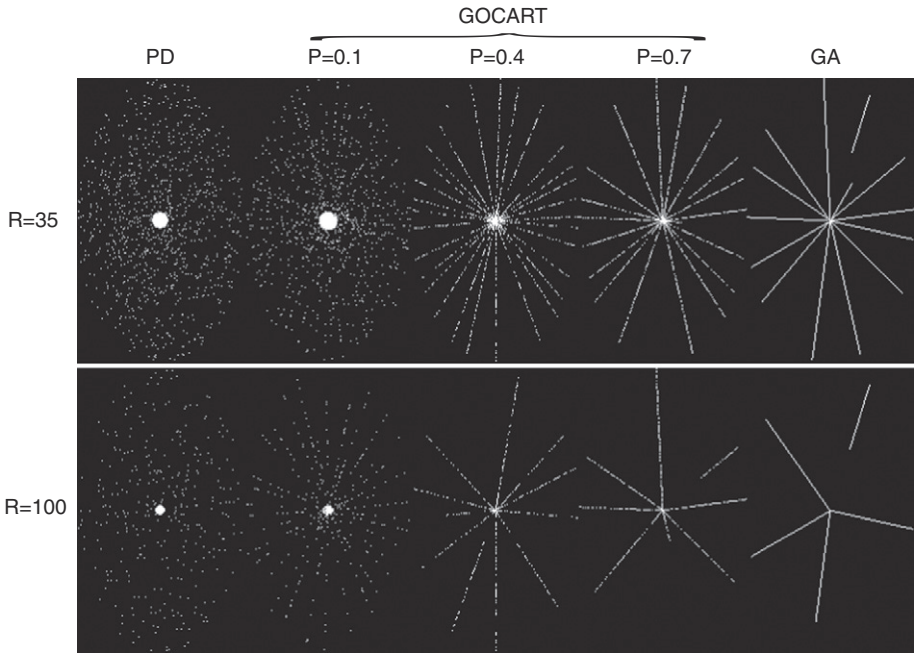

Fig. 1. Sampling pattern (k_y,k_z) for single time frames for PD, GOCART with P equal to 0.1, 0.4, 0.7, and 1 (GA), when the reduction factor (R) equals to 35× (top row) and 100× (bottom row). The matrix size is 256 × 150, the P = 1 central regions account for approximately 15% of PEs, and the temporal window W was empirically set to 70% of the undersampled temporal resolution to limit the PE redundancy. As P decreases, the sampling pattern appears more random, and there are fewer large gaps in k-space.

sampling [25] has been a popular choice for undersampling since compressed sensing was introduced to MRI [24]. Numerous algorithms have been proposed for efficiently generating Poisson disc sampling patterns, including dart throwing [26], jittered sampling [27], best candidate [28], and more recent O(N) boundary sampling [29] and modified dart throwing [30]. Of relevance to this work, Lebel et al. [15] proposed Poisson ellipsoid sampling based on dart-throwing for dynamic imaging by extending the 2D Poisson disc pattern to 3D k_y-k_z-t space. This method provides excellent transform sparsity, is compatible with parallel imaging, and limits temporal redundancy. Unfortunately, it is computationally intensive, has many input variables, and is poorly suited to variable temporal resolution. In contrast, golden angle Cartesian sampling [19] provides more coherent sampling than the Poisson ellipsoid approach, but allows flexibility in the specification of temporal resolution during reconstruction and allows for fast on-line generation of the phase encode order. Here we denote ***PD*** to variable density Poisson ellipsoid sampling and ***GA*** to Cartesian golden angle radial sampling. We propose a modified GA approach that combines the benefits of PD and GA. We introduce a sampling probability, via pseudorandom number generation, to add additional incoherence to GA [31]. The proposed approach is termed as GOlden-angle CArtesian Randomized Time-resolved (GOCART) 3D MRI.

Methods

Data acquisition phase encode ordering

We have implemented continuous data acquisition by modifying a standard 3D Cartesian spoiled gradient echo sequence, where full Cartesian sampling is used along the standard frequency encoding direction k_x, and PE sampling in the k_y-k_z plane can be freely sub-sampled and/or reordered.

Poisson disc sampling has been shown to be suitable for combined parallel imaging and compressed sensing. Poisson ellipsoid [15] expands Poisson disc to k_y-k_z-t space with the constraint that samples do not coexist within an ellipsoid surrounding each sample. Variable density is achieved by subdividing the k_y-k_z plane into a series of annuli with exponentially decreasing sampling density, and fully sampling central region with 15% of the total samples.

Golden angle sampling [32] supports flexible temporal resolution selection in reconstruction because it provides approximately uniform angular sampling for an arbitrary number of spokes. 3D Cartesian GA implementation [19] is applied in the k_y-k_z plane, where Cartesian PEs are selected in order to form a close approximation to golden angle radial spokes.

Based on the GA scheme, we introduce a probability of sampling (P) for each PE, a central k-space region where P always equals to 1, and a temporal window (W) within which the same PE is not repeated. Once a PE is chosen by a GA radial spoke going through it, the chance of acquisition is determined by P ($P \in (0, 1]$), such that part of the PEs along the spoke is skipped. The logical next step is that we can acquire data from subsequent spokes by skipping some PEs in one spoke, and achieve more incoherent and uniform sampling. PE skipping is disabled (P = 1) within a predefined central region because the center of k-space is especially important for preserving low-frequency image information. Considering that each spoke starts from (or ends in) the center of k-space, the center is naturally oversampled, and excessive k-space center sampling density needs to be avoided. The temporal window W prevents frequently repeated PEs, and the window width is defined as integer multiple of the TR. Finally, we do not acquire the corners of the k_y-k_z plane.

Fig. 1 demonstrates the PEs for single time frames for PD, GOCART with P = 0.1, 0.4, 0.7, and 1 (equivalent to the original GA). It is worth noting that data are continually acquired and retrospectively binned into frames for reconstruction. Within each data frame, the first PE and the last PE may be in the middle of radial spokes, which look like a discontinuity in the k_y,k_z plane (e.g. GA with R = 35 in Fig. 1). Reduction factors (R) of 35× and 100× are presented for a matrix size of 256 × 150. The P = 1 central regions account for approximately 15% of PEs at each undersampling, in accordance with the setting in PD. W was empirically set to 50% of the number of PEs per time frame with 100× acceleration to limit sampling redundancy.

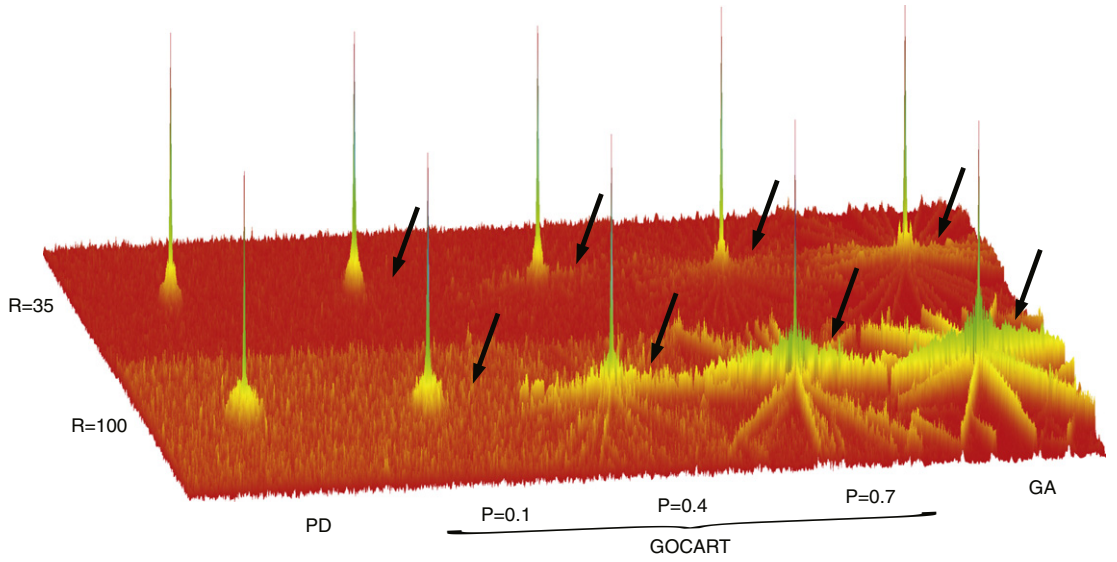

Fig. 2. Point spread functions (PSF) for the sampling patterns in Fig. 1. High acceleration rates have more pronounced side lobes than lower rates. GA (i.e., GOCART with P = 1.0) has undersampling artifacts concentrated in clearly visible streaking patterns. The streaking side lobes are effectively attenuated by reducing the sampling probability (P). As P approaches 0, the PSFs closely resemble those obtained with PD.

35× is used in our current experimental DCE setup, and 100× is the highest R in this study. As P decreases, more sampling randomization is achieved, and the central region has better coverage.

Constrained reconstruction

We employed a sparse SENSE image model [33,34] with multiple constraints applied as l_1-norm penalties. The image m is obtained by minimizing

$$f(m) = \|F_u S m - y\|_2^2 + \lambda_1 \|T_t m\|_1 + \lambda_2 \|T_s m\|_1 + \lambda_3 \|\psi m\|_1 \quad (1)$$

where F_u is the undersampling Fourier operator, S is the sensitivity operator, y is the acquired k-space data, T_t is the temporal finite difference, T_s is spatial finite difference, and ψ is the spatial wavelet transform. λ's were carefully chosen to avoid compression artifacts and maintain high data consistency. Once calibrated, λ's were held constant for all other brain DCE-MRI studies. λ_2 and λ_3 were set to zero in in-vivo retrospective studies and phantom simulations to calibrate and validate the GOCART method. This was done to reduce uncertainties that may be induced from multiple constraints. Multiple constraints are used in in-vivo prospective studies to lessen the burden on individual constraints and minimize compression artifacts due to each transformation [15]. The cost function in Eq. (1) was minimized with an augmented Lagrangian method [35], alternating direction methods of multipliers (ADMM).

Experiments

Point spread function analysis

The sampling probability P is a key feature of GOCART and analyzing image-space point spread functions (PSF) provides an intuitive metric for optimizing this parameter. The aim is to reduce coherent side lobes, which is expected to improve compatibility with compressed sensing [24]. The PD sampling tables were always generated separately for different temporal resolutions, while GA and GOCART sampling tables were retrospectively segmented from single generations, respectively. The PSFs were obtained by taking inverse Fourier transforms along the k_y-k_z dimensions. All the PSFs were normalized to the peaks, and displayed at the same linear scale.

Retrospective in-vivo studies

Fully sampled DCE data from five brain tumor patients were acquired on a clinical 3 T scanner (HDxt, GE Healthcare, Waukesha, WI) using an 8-channel head coil and T1-weighted spoiled gradient echo sequence with 15° flip angle and 6 ms TR. Each subject was screened and provided informed consent in accordance with institutional policy. The conventional DCE data had two sizes: A) three datasets with 256 × 186 × 10 matrix size and 24 × 24 × 6 cm^3 FOV, and B) two datasets with 256 × 150 × 10 matrix size and 22 × 22 × 6 cm^3 FOV. All the data had 35 time frames with approximately 10 s temporal resolution.

In our 3D undersampling sequence, the readout direction k_x is always fully sampled, and constrained reconstruction is effectively recovering samples in the k_y-k_z plane. Therefore, we fabricated k_y-k_z-t data from fully sampled k_x-k_y-t data acquired from conventional DCE protocol, and performed retrospective studies using the k_y-k_z-t data. In this way, we obtained a fully sampled reference scan with sufficient temporal resolution. A single slice from each conventional DCE dataset was used to synthesize k_y-k_z-t data. The data were retrospectively downsampled using PD, GA and GOCART schemes at 20 different R's evenly distributed between 5× and 100×. To prevent bias, we generated 50 sampling patterns for each scheme by altering the pseudorandom generator seeds (PD, GOCART) and/or initial angles (GA, GOCART). The pharmacokinetic (PK) parameter K^{trans} was calculated for tumor ROIs, and the agreement of K^{trans} was assessed using concordance correlation coefficients (CCCs) and Bland–Altman plots. The results of tumor and vessel regions of interest (ROI) were quantitatively assessed using normalized root-mean-squared-error (nRMSE) between the reconstructed and fully sampled reference images.

Phantom simulation studies

We manually segmented post-contrast whole-brain DCE-MRI data [15] from a brain tumor patient into five non-overlapping regions: vessels, tumor boundary, tumor core, cerebrospinal fluid (CSF), and other tissue. K^{trans} of tumor boundary and tumor core was

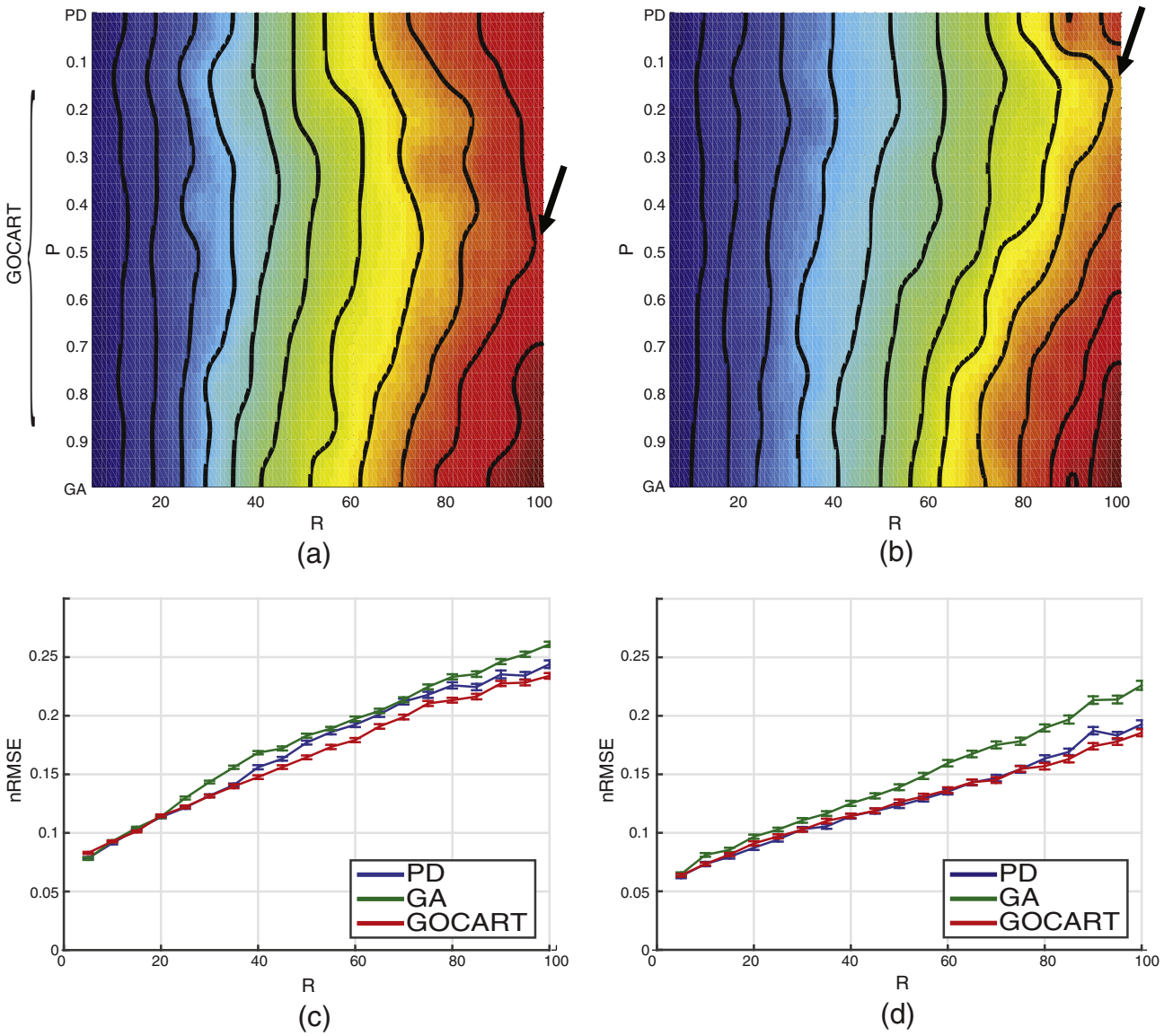

Fig. 3. Mean nRMSE of (a) tumor ROI, and (b) vessel ROI with contours outlining equivalent nRMSE. The two axes are reduction factor R and sampling probability (P) ranging from 5× to 100× and 0 to 1, respectively. PD is plotted as P = 0 for the convenience of comparison. GOCART is advantageous with large R (arrows). The mean and standard deviation comparison of PD, GA and GOCART (P = 0.3) with respect to R are shown for (c) tumor ROI and (d) vessel ROI. On the tumor, GOCART outperforms PD and GA with R > 35; on the vessel, GOCART beats GA in all cases, and outperforms PD with R > 75. The standard deviations are small (<3%) compared with the means.

0.1 and 0.02 min^{-1}, respectively, which mimicked our in-vivo estimates. Other PK parameters, including v_p, v_e and tissue T_1, were given literature values for each region [36,37]. A population-based arterial input function (AIF) [38], a two-compartment exchange model [36], and the steady state spoiled gradient signal equation, were used to generate the time intensity curves and fabricate dynamic images. We then multiplied coil sensitivities, took the Fourier transform, and added realistic noises. Coil sensitivity maps, noise covariance matrix and signal-to-noise ratio were estimated from the in-vivo data. B_1^+ variation and T_2^* decay were not modeled, but could be included later.

The phantom had a 256 × 256 × 100 matrix size and a 24 × 24 × 19 cm^3 FOV, identical to those of the acquisition protocol for experimental prospective in-vivo data. We simulated a TR by TR acquisition with TR = 6 ms for a 10-min period (100,000 TRs). One single axial slice of size 256 × 100 was used to synthesize k_y-k_z-t data acquired using PD, GA and GOCART at R = 35 and R = 100. PD has no flexible temporal resolution in the reconstruction, therefore, the PE ordering of PD at R = 100 was separately generated. nRMSE was also used to quantitatively compare the results.

Prospective in-vivo studies

Two prospective GOCART undersampled data were acquired from brain tumor patients. Informed consent was obtained from patients prior to MRI scans. Our institutional review board approved these studies.

Patient data were acquired using an 8-channel head coil and an axial T1-weighted spoiled gradient echo sequence with 15° flip angle and 6 ms TR. The data had 256 × 256 × 100 matrix size and 22 × 22 × 19 cm^3 FOV. Prior to each scan, T1 maps were acquired using a variable flip angle DESPOT1 method [39]. Multiple constraints (Eq. (1)) with empirical λ values were employed [15]. After image reconstruction, a Patlak model [40] was used to estimate PK parameters. The AIF was generated from a population-averaged analytic equation [38].

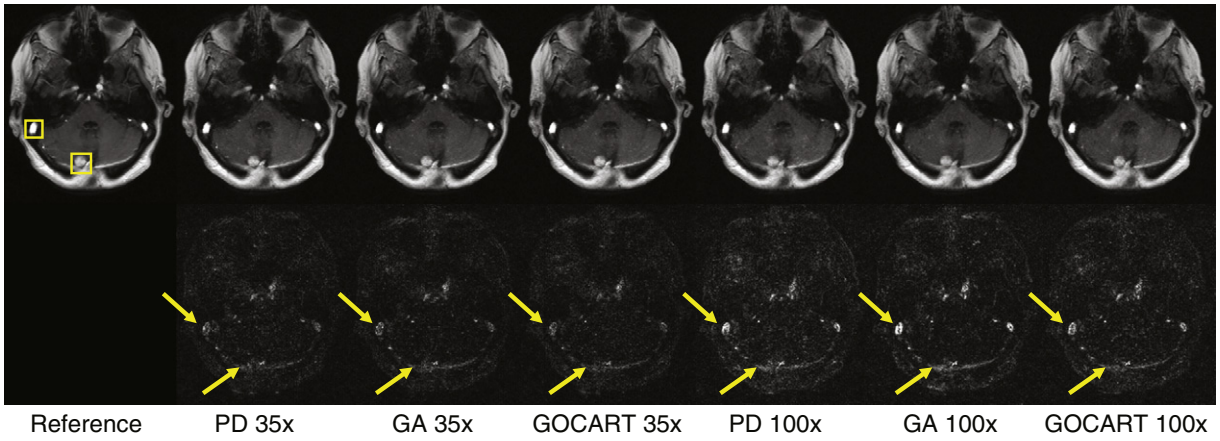

Fig. 4. A single time frame during peak enhancement from a meningioma patient. Tumor and vessel regions are identified in the fully sampled reference image. Results of PD, GA and GOCART (P = 0.3) are shown at R equals 35× and 100× (as labeled). The second row displays the difference images between the reference and reconstructed undersampled images (intensity scaled by 3). GA results in higher errors in vessels than PD and GOCART especially when R = 100 (upper arrows). All these three methods performed similarly well with the tumor, except PD yielded slightly higher error when R = 100 (lower arrows).

Results

Fig. 2 shows the PSFs of the sampling patterns in Fig. 1. In general R = 100 has higher side lobes than R = 35. PD has the lowest amplitude lobes while GA (which is GOCART with P = 1) has clearly visible coherent streaks. With GOCART, this coherent streaking diminishes as P decreases (arrows), essentially converging to PD as P approaches 0. All the PSFs were normalized to the peaks, and the minor visible peak differences are due to interpolation.

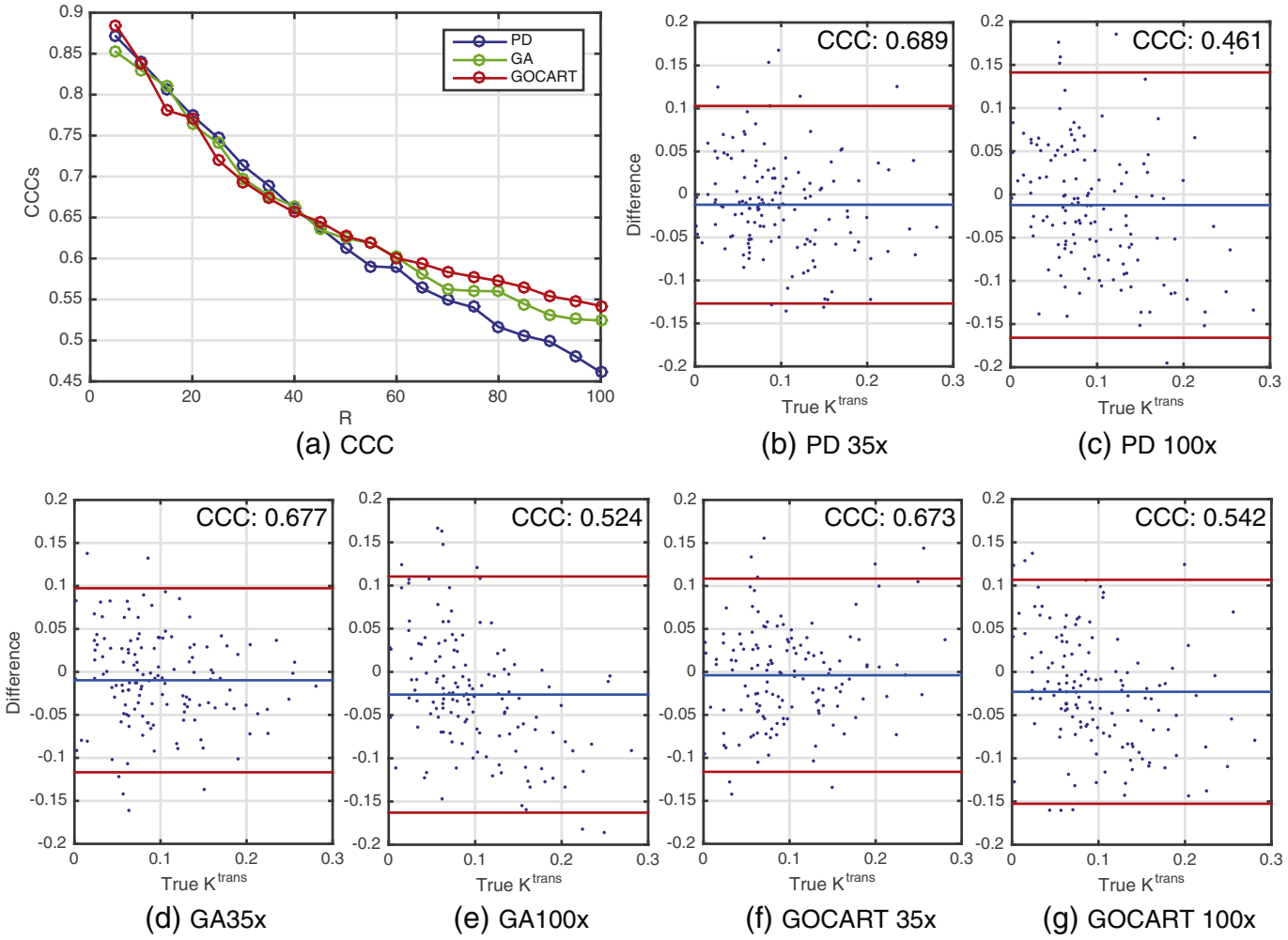

Fig. 5. (a) CCCs of the same dataset changes as a function of R. All three techniques perform similarly when R < 50, and GOCART outperform PD and GA when R > 50. (b-g) Bland–Altman plots and 95% confidence intervals within two red lines. CCCs at R = 100 in general have larger bias and variance than CCCs at R = 35. PD, GA and GOCART produce similar confidence intervals at R = 35, and PD results in larger variance but smaller bias than GA and GOCART at R = 100. (For interpretation of the references to color in this figure legend, the reader is referred to the web version of this article.)

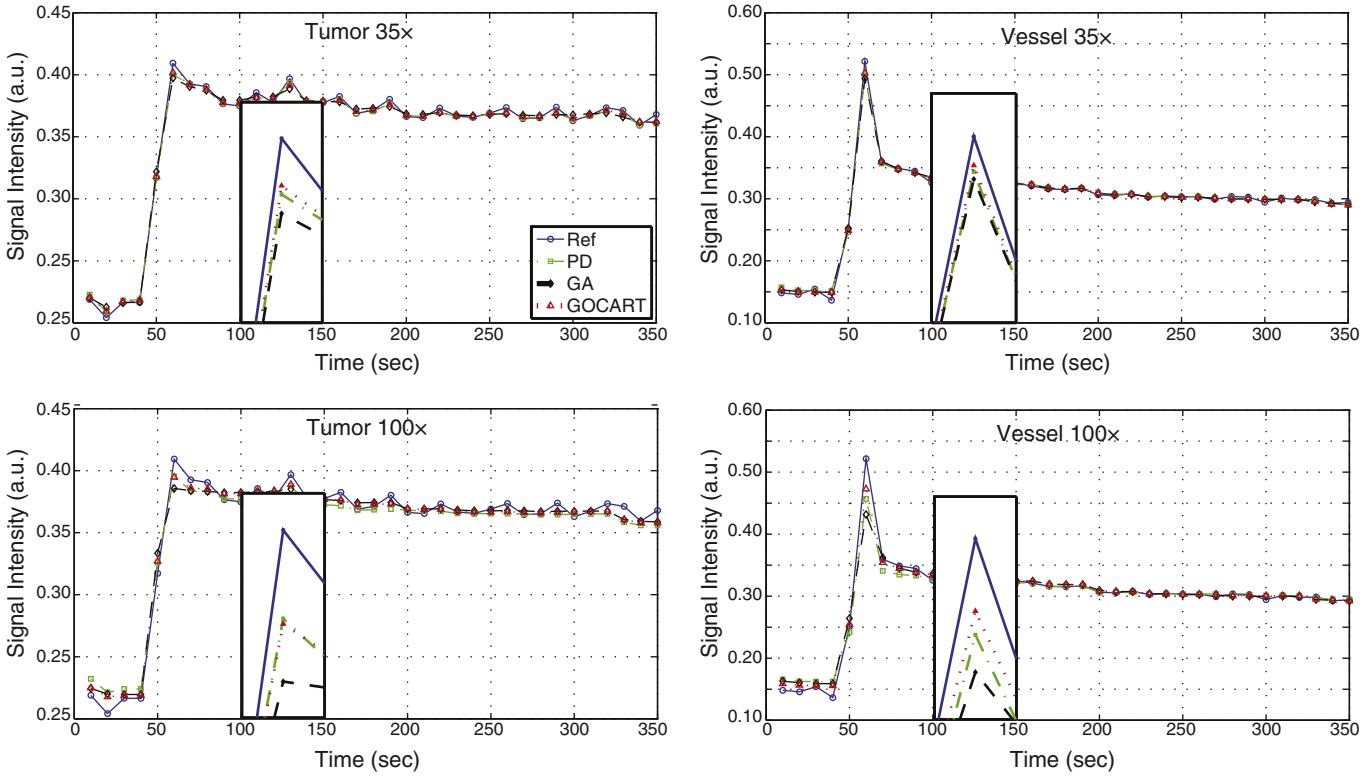

Fig. 6. The time-intensity curves (TIC) of reconstructed results of the data in Fig. 4. The TICs of reference, R = 35 and R = 100 were averaged from tumor and vessel ROI (as labeled). Data fidelity is maintained better at 35× compared to 100×. GOCART yielded peak signals that are closest to reference, except in tumor with R = 100 (Figure 6 lower left subfigure), GOCART peak is slightly (0.3%) lower than PD peak. Overall, GOCART provided the highest temporal fidelity in the comparison group.

Fig. 3(a,b) illustrates the mean nRMSE of tumor and vessel ROIs, respectively. nRMSE was averaged from 50 datasets over five patients, and the equivalent results were connected into contour lines (isolines). The two axes are R and P ranging from 5× to 100× and 0 to 1, respectively. Here we plotted PD as P = 0 for the convenience of comparison. Reconstruction error in large, multi-voxel tumors and small vessels was insensitive to sampling schemes with acceleration rates below 20×. GOCART is advantageous over PD or GA because it has lower nRMSE at higher acceleration rates (arrows). Tumors with structures and smooth signal variation were most accurately reconstructed with the moderate randomization obtained with P between 0.3 and 0.5; small, tiny vessels with rapidly changing signal were most accurately recuperated with additional randomization using $0.1 < P < 0.3$. As such, P = 0.3 was selected as a compromise and was used for subsequent experiments. The mean and standard deviation comparison of PD, GA and GOCART (P = 0.3) with respect to R is shown for tumor and vessel ROIs in Fig. 3(c,d), respectively. On the tumor, GOCART outperforms PD and GA with $R > 35$; on the vessel, GOCART overtakes GA in all cases, and outperforms PD with $R > 75$. The standard deviations are small (<3%) compared to the means in all cases.

Fig. 4 contains a single time frame during peak enhancement from a meningioma patient. The tumor and vessel ROIs are shown in the reference image. These results were reconstructed from the same reference data but retrospectively undersampled with PD, GA and GOCART (P = 0.3) at R = 35 and 100 (labeled). No residual aliasing artifacts are visually apparent and no reduction in effective resolution is seen, as evidenced by images on the first row. Difference images between the reference and reconstructed under-sampled images (intensity scaled by 3) indicate that the errors mainly occur in vessels with abrupt spatial/temporal signal changes. GA results in higher error in vessels than PD or GOCART, especially when R = 100 (upper arrows). All three methods performed well within the tumor, but GOCART yielded slightly lower error at R = 100 than the other methods (lower arrows), as predicted in Fig. 3.

Fig. 5(a) demonstrates CCCs of the same dataset changes as a function of R. As R increases from 5 to 100, CCCs of PD, GA and GOCART decrease from above 0.85 to below 0.55. All three techniques perform similarly when $R < 50$, and GOCART outperform PD and GA when $R > 50$. Fig. 5(b-g) presents Bland–Altman plots with horizontal axis presenting true K^{trans} values, and vertical axis presenting K^{trans} differences. The blue line in the middle is the average value of the differences, and the two red lines provide 95% confidence intervals (within average ± 1.96 standard deviation of the differences). CCCs at R = 100 in general have larger bias and variance than CCCs at R = 35. PD, GA and GOCART produce similar confidence intervals at R = 35, and PD resulted in larger variance but smaller bias than GA and GOCART at R = 100.

Fig. 6 shows the time-intensity curves (TIC) of reconstructed results of the data in Fig. 4. The TICs of R = 35 and R = 100 were averaged from tumor and vessel ROIs (as labeled) to avoid bias of choosing single voxel. The signal peak regions are critical for PK parameter estimation, and are enlarged in each plot. GOCART yielded peak signals that are closest to reference, except in tumor with R = 100 (Fig. 6 lower left subfigure), where GOCART peak is slightly (0.3%) lower than PD peak. Similar results were observed on all the other datasets, which are not shown. Overall, GOCART provided the highest temporal fidelity in the comparison group.

Fig. 7 demonstrates the phantom experiment outcomes. Fig. 7(a) is the manually segmented phantom, and the time-varying vessel, tumor boundary and tumor core are labeled. Fig. 7(b,c) demonstrates the reconstructed TICs of these three ROIs. The ground truth (reference) is shown with a smooth blue line because it has 6 ms temporal resolution, and the temporal resolution of R = 35 and

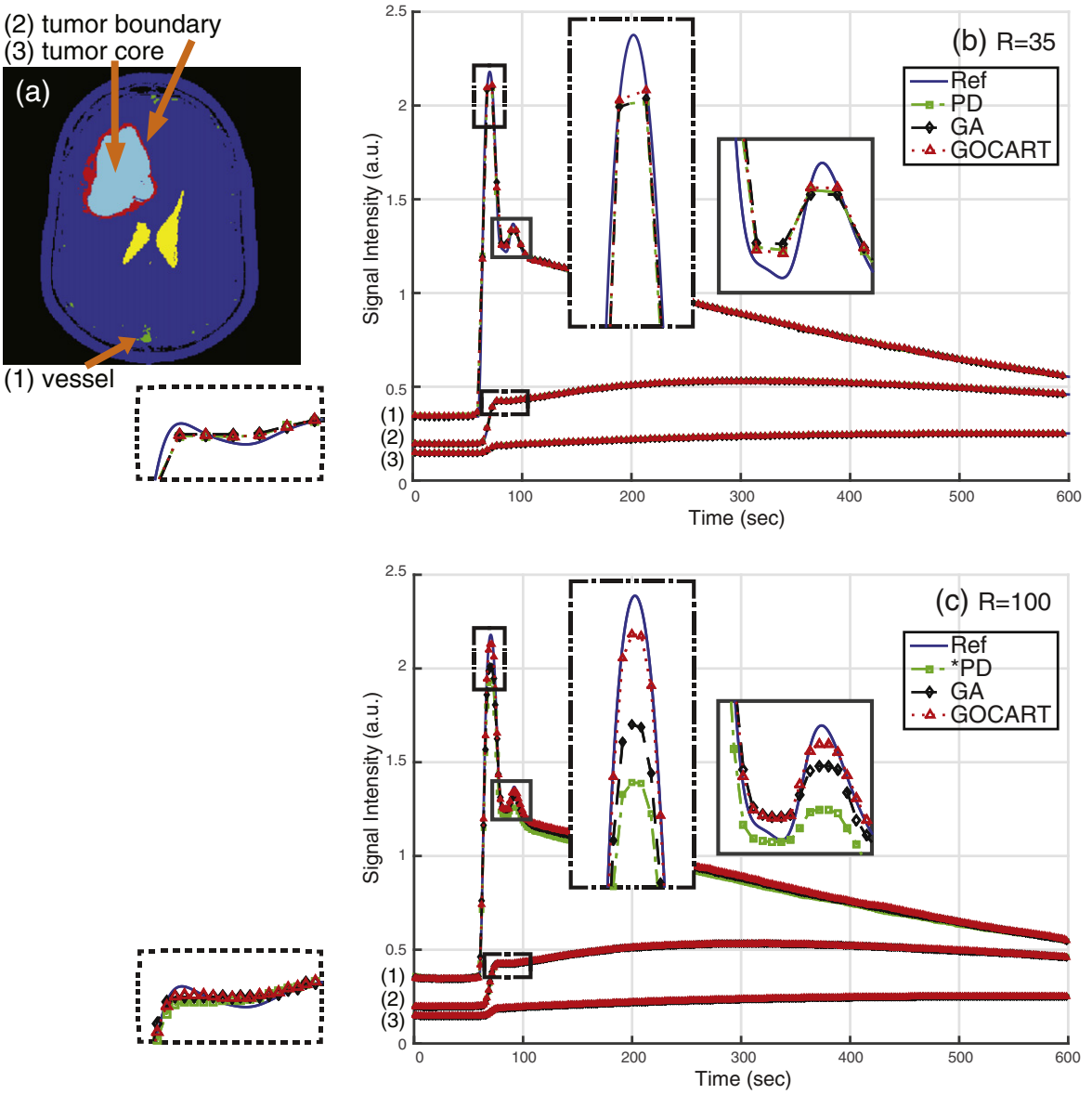

Fig. 7. (a) Manual phantom segmentation results. The vessel, tumor boundary and tumor core were time-varying in the simulation. (b, c) Reference and reconstructed TICs of the three ROIs at R = 35 and R = 100, respectively. The PD sampling at R = 100 was regenerated independently. The reconstructed signal peak regions of vessel and tumor boundary are enlarged for visualization. Although worse than PD at R = 35, GOCART beat GA in both accelerations, and GOCART at R = 100 recuperated the most accurate peak signal shapes and peak signal arrival times.

R = 100 was 4.39 s and 1.54 s, respectively. The vessel nRMSE of PD, GA and GOCART at R = 35 were 0.90%, 1.16% and 0.89%, respectively, and at R = 100 were 3.91%, 2.08% and 0.85%, respectively. There was no apparent difference in reconstructed images of tumors, where the signals were slowly varying. The reconstructed signal peaks of vessel and tumor boundaries are enlarged for visualization. Notice that the corresponding enlarged regions have exactly the same display rage for R = 35 and R = 100. GOCART most accurately recuperated the varying signals, especially when R was large and the signals had abrupt changes.

The DCE-MRI was reconstructed with a net acceleration factor of 35× and temporal resolution of 4.5 s, the same as current clinical protocol. Fig. 8 shows representative GOCART results with 4 temporal phases obtained on (a) a left posterior fossa meningioma patient and (b) a right-sided acoustic schwannoma patient, respectively. The tumors are arrowed in the last figures where the tumor enhancement was maximal. The temporal evolutions of these two tumors are provided in two Supplementary videos.

Fig. 9(a,b) presents permeability K^{trans} maps calculated from GOCART prospective results from the left posterior fossa meningioma patient and right-sided acoustic schwannoma patient, respectively (raw images in Fig. 8). The K^{trans} maps appear as expected: higher blood brain barrier is observed in the tumor tissues (arrows), and acoustic schwannoma has significant BBB permeability. No leakage is observed in the healthy parenchyma.

The CE-MRA was reconstructed with net acceleration factor of 100× to demonstrate the flexibly temporal resolution of GOCART. Our retrospective in-vivo studies (Fig. 6) and phantom simulations (Fig. 7) have indicated that GOCART is most advantageous at highly accelerated vascular imaging. Fig. 10 demonstrates maximum intensity projection (MIP) of right-sided acoustic schwannoma patient on (a) sagittal and (b) axial planes. Four reprehensive time

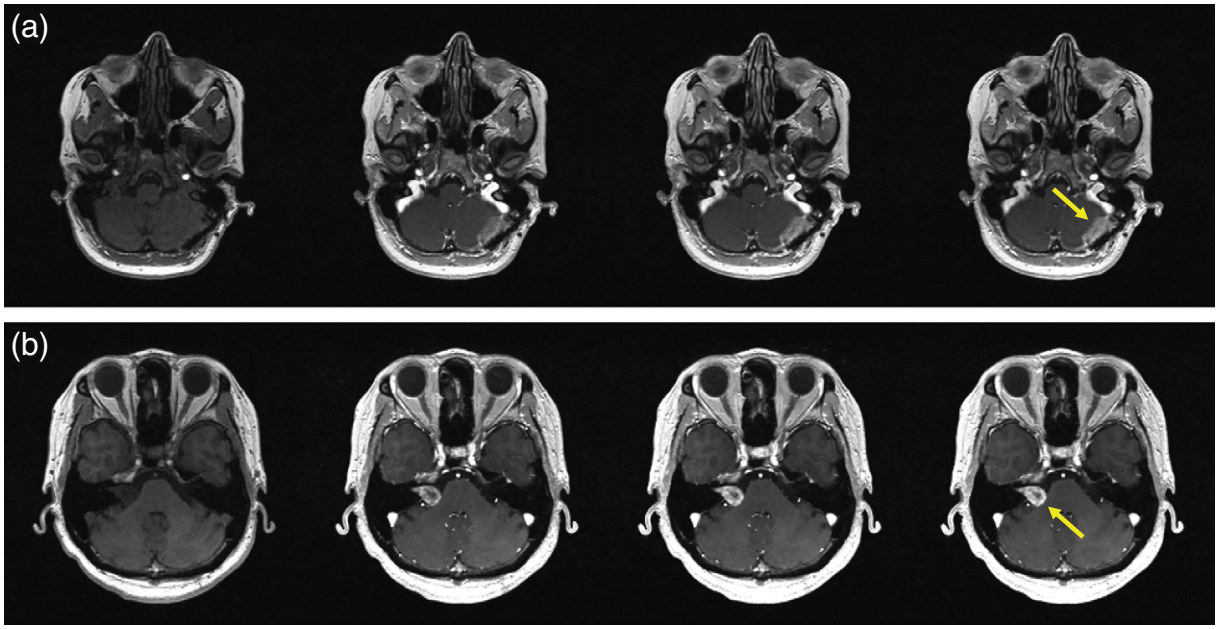

Fig. 8. Representative results with 4 temporal phases obtained on (a) a patient with a left posterior fossa meningioma and (b) a patient with a right-sided acoustic schwannoma. The tumors are arrowed in the last figures where the tumor enhancement was maximal. The temporal resolution was 4.5 s and the net acceleration was 35 × .

frames from 33 s, 41 s 86 s and 131 s illustrate the dynamic pass of the contrast agent in the intracranial vessels. The acoustic schwannoma can be clearly visualized in the axial MIP (arrows). Rotating MIP maps as time progress are provided in Supplementary videos.

Fig. 11 contains axial post-gadolinium T1-weighted images of the right-sided acoustic schwannoma, from inferior to superior. These images are the last time frame reconstructed from prospective GOCART undersampled data. The tumor has been fully enhanced by the contrast bolus. The high resolution GOCART imaging protocol evidently depicts the shape and fine details of the acoustic schwanoma, as pointed out by the arrows.

Discussion

GOCART is a novel sparse sampling scheme for time-resolved 3D Cartesian MRI. GOCART combines the best components of GA and PD: GOCART samples the center of k-space very frequently, distributes PEs uniformly throughout the sampling domain (via the ergodic nature of GA), and locally randomizes sampling locations. We have performed retrospective validation on fully sampled in-vivo data and phantom simulation, where the ground truth can be defined for image quality assessment. We have demonstrated that GOCART is favorable for 3D DCE-MRI using constrained reconstruc-

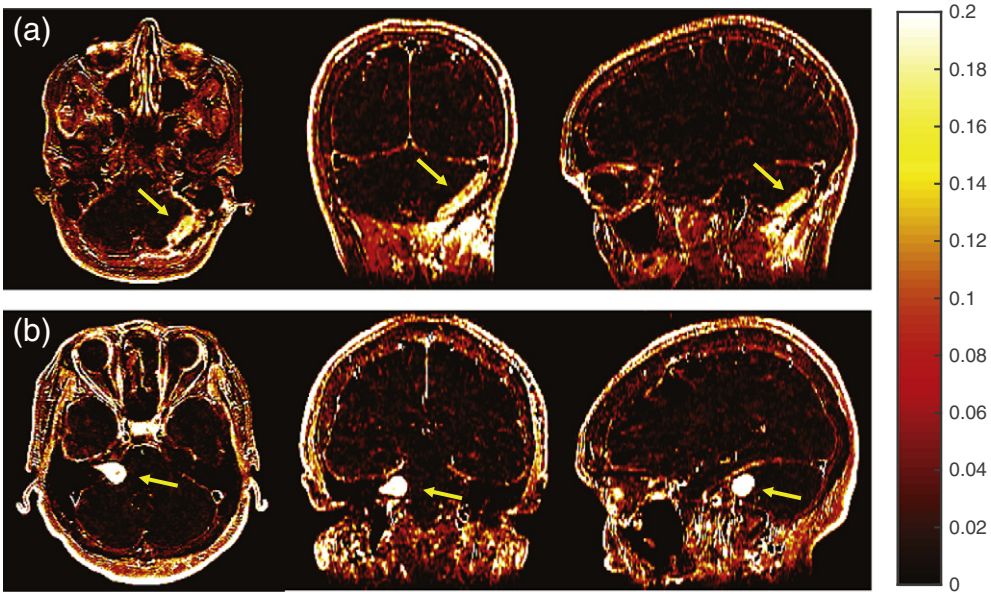

Fig. 9. K^{trans} maps calculated from (a) a patient with a left posterior fossa meningioma and (b) a patient with a right-sided acoustic schwannoma (raw images in Fig. 8). The K^{trans} maps clearly show significantly higher permeability and leakiness of the blood brain barrier in the tumor tissues (arrows). No leakage is observed in the healthy parenchyma.

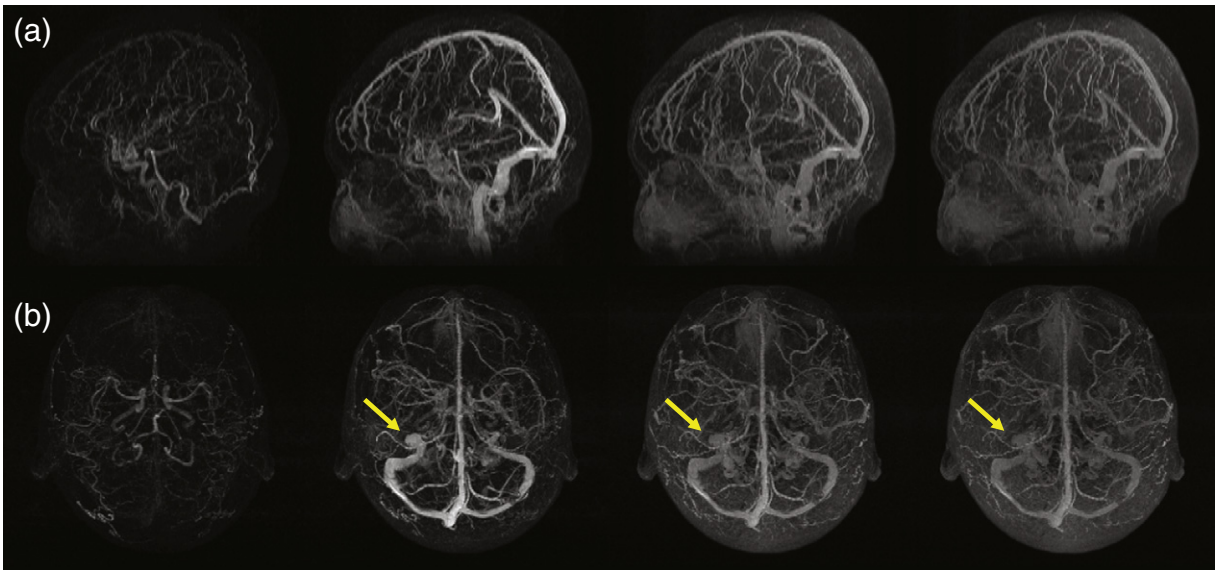

Fig. 10. Maximum intensity projection (MIP) of acoustic schwannoma patient on (a) sagittal and (b) axial planes. The image series was reconstructed with net acceleration factor of 100× to demonstrate the flexibly temporal resolution of GOCART. Five reprehensive time frames from 23 s, 33 s, 41 s 86 s and 131 s illustrate the dynamic pass of the contrast agent in the intracranial vessels. The acoustic schwannoma can be clearly visualized in the axial MIP (arrows).

tion. We have shown the strengths of GOCART and its potential impact on brain DCE MRI.

GOCART has five important advantages: 1) GOCART allows fast, flexible, and reproducible case-dependent view-order generation. It required 0.097 s for GOCART and 31 s for PD to generate sampling patterns for a 10 min DCE scan on a single 2.5 GHz CPU. GOCART is therefore suitable to real-time selection of imaging parameters such as the FOV and spatial resolution. With a suitable pseudo-random number generator, the sampling pattern can be readily re-generated during image reconstruction, eliminating storage and transfer of an external look-up table. 2) GOCART maintains or improves reconstruction accuracy and temporal resolution relative to alternative methods. In no case did GOCART overly degrade reconstructed image quality and in some cases, specifically very high acceleration rates, outperformed PD and GA. These have been demonstrated in both retrospective in-vivo studies and phantom simulation studies. 3) As it is based on a radial acquisition, GOCART has intrinsic variable density sampling. The underlying sampling density is inversely proportional to k_r, the radial distance to the k-space center. The center of k-space has higher sampling density, which is beneficial for sparse reconstruction [15,24]. 4) GOCART inherits the flexible temporal resolution intrinsic to GA. The optimal temporal resolution for a dynamic MRI scan is often unknown *a priori* and depends on the PK parameters of the tissue. The phantom simulation also suggested a variable temporal resolution reconstruction that assigns a higher temporal resolution to significantly changing signals. This is possible with GOCART. 5) Although not shown in this work, GOCART is compatible with multi-level sampling patterns that leverage

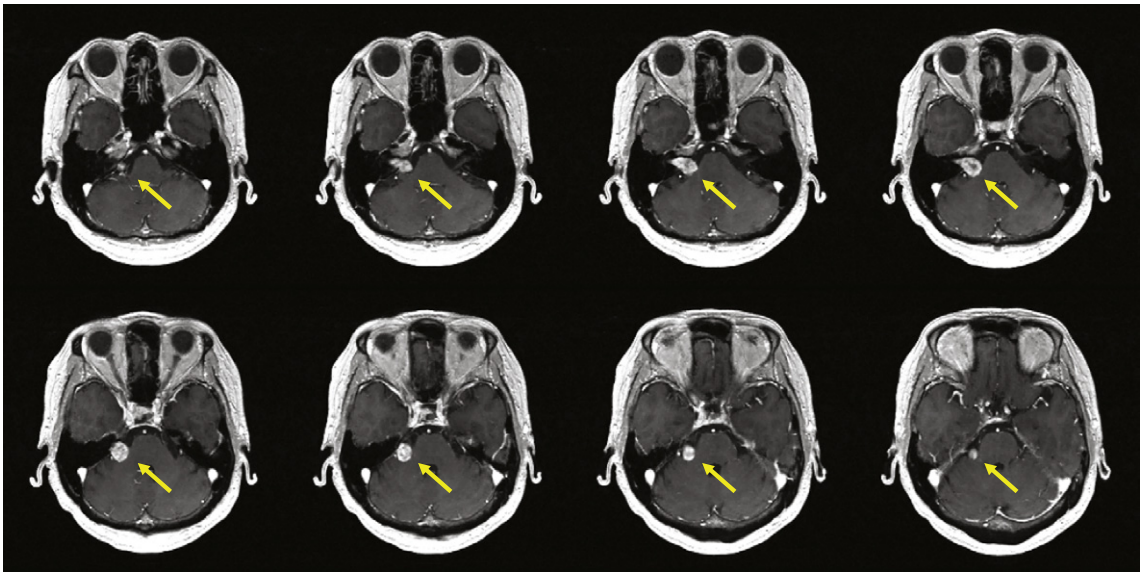

Fig. 11. Axial post-gadolinium T1-weighted images of the right-sided acoustic schwannoma, from inferior to superior. The tumor has been fully enhanced by the contrast bolus. The arrows point out the evident depiction of the acoustic schwanoma by our high resolution GOCART imaging protocol.

asymptotic structure in CS and are tailored to the object [41]. Specifically, a k_r-dependent sampling probability mask can be employed, instead of a uniform sampling probability.

GOCART bears similarities and thus shares some of the aforementioned advantages with recently proposed methods such as TWIST [11], IVD [12], DISCO [14] and VDRad [20], which have been used in other contrast enhanced applications. For instance, $1/k_r$ variable density undersampling is similar to IVD and VDRad, and predefining a $P = 1$ central region is similar to TWIST and DISCO. Besides, TWIST, IVD, DISCO and VDRad combine adjacent frames to form a fully sampled footprint; GOCART can generate similar footprint, although fully sampling is not always guaranteed. GOCART has enhanced variable temporal resolution ability from more uniform samples. A wider range of temporal resolution selections facilitates exploring optimal experiment designs for different PK performances and capturing the signal peaks, perhaps making GOCART better suited for brain DCE MRI.

The classical temporal finite difference was chosen because of its simplicity (convex optimization, single tuning parameter, appropriateness for DCE-MRI). We agree that data-driven reconstruction algorithms such as k-t SLR [42], and blind compressed sensing [43] may offer improved reconstruction performance. However, these were not considered in this study, as these schemes are associated with increased complexity (non-convex optimization, non-trivial tuning of free parameters, convergence not guaranteed and will depend on the sampling pattern).

Our experiment design has a number of limitations. In the retrospective in-vivo studies, the reference data with approximately 10 s temporal resolution were used as snapshot, which is not ideal especially for fast varying signals. In addition, the retrospective in-vivo data suffered from some inflow artifacts. In the phantom simulation studies, data at 6 ms temporal resolution were generated and scanner data acquisition was simulated. However, we could have achieved such high acceleration factors because the phantom lacked sufficient anatomical detail. Furthermore, the calibrated λ'*s* were different in retrospective in-vivo studies and phantom simulation studies, and we empirically chose λ'*s* from retrospective in-vivo studies for prospective in-vivo studies. Neither of the experiments was able to test the effect of eddy currents, which may be more noticeable as the sampling probability decreases. Acquiring radial spokes from the edge of k-space toward the center rather than center out may mitigate this effect.

One potential improvement may be achieved by taking full advantage of head coil geometry with parallel imaging. The 8 elements of our head coil provide maximum diversity in the axial plane, which was the phase encoding plane in the prospective whole-brain DCE-MRI experiments. Although not specifically done in this work, it is possible to optimize GOCART for parallel imaging by incorporating structured undersampling along spokes, as seen in IVD [12] or DISCO [14]. This is also true for PD and GA.

GOCART outperformed PD and GA in both retrospective in-vivo studies and phantom simulation studies. However, PD generally outperformed GA in the former studies but was overtaken in the later ones. This is likely due to the fact that GA samples the center of k-space more frequently within temporal windows.

We have compared GOCART with PD and GA through retrospective analysis and phantom simulation, and have shown prospective in-vivo clinical results. Our results demonstrate that GOCART has combined the advantages of both PD and GA, and outperforms both techniques in highly undersampled cases. We provide the source code for GOCART on http://mrel.usc.edu/sharing/GOCART.zip, which includes both Matlab and C implementations, and has additional optional features such as golden angle adjustment for anisotropic FOV and angular perturbation that were not used in this study.

Supplementary data to this article can be found online at http://dx.doi.org/10.1016/j.mri.2015.12.030.

Acknowledgements

The authors would like to thank Dr. Angel Pineda for useful discussion on image quality evaluation in constrained reconstruction, and Samuel Valencerina for assistance collecting raw DCE-MRI data from brain tumor patients. This research was partially supported by the National Center for Advancing Translational Sciences of the National Institutes of Health under Award Number UL1TR000130 (formerly by the National Center for Research Resources, Award Number UL1RR031986). The content is solely the responsibility of the authors and does not necessarily represent the official views of the National Institutes of Health. The retrospective experiments were partly performed at the Center for High Performance Computing of the University of Southern California.

References

[1] Van Vaals JJ, Brummer ME, Dixon WT, Tuithof HH, Engels H, Nelson RC, et al. "Keyhole" method for accelerating imaging of contrast agent uptake. J Magn Reson Imaging 1993;3:671–5.
[2] Korosec FR, Frayne R, Grist TM, Mistretta CA. Time-resolved contrast-enhanced 3D MR angiography. Magn Reson Med 1996;36:345–51. http://dx.doi.org/10.1002/mrm.1910360304.
[3] Vigen KK, Peters DC, Grist TM, Block WF, Mistretta CA. Undersampled projection-reconstruction imaging for time-resolved contrast-enhanced imaging. Magn Reson Med 2000;43:170–6.
[4] Du J, Bydder M. High-resolution time-resolved contrast-enhanced MR abdominal and pulmonary angiography using a spiral-TRICKS sequence. Magn Reson Med 2007;58:631–5. http://dx.doi.org/10.1002/mrm.21298.
[5] Song HK, Dougherty L. Dynamic MRI with projection reconstruction and KWIC processing for simultaneous high spatial and temporal resolution. Magn Reson Med 2004;52:815–24. http://dx.doi.org/10.1002/mrm.20237.
[6] Feng L, Grimm R, Block KT, Chandarana H, Kim S, Xu J, et al. Golden-angle radial sparse parallel MRI: combination of compressed sensing, parallel imaging, and golden-angle radial sampling for fast and flexible dynamic volumetric MRI. Magn Reson Med 2014;72:707–17. http://dx.doi.org/10.1002/mrm.24980.
[7] Barger AV, Block WF, Toropov Y, Grist TM, Mistretta CA. Time-resolved contrast-enhanced imaging with isotropic resolution and broad coverage using an undersampled 3D projection trajectory. Magn Reson Med 2002;48:297–305. http://dx.doi.org/10.1002/mrm.10212.
[8] Mistretta CA, Wieben O, Velikina J, Block W, Perry J, Wu Y, et al. Highly constrained backprojection for time-resolved MRI. Magn Reson Med 2006;55:30–40. http://dx.doi.org/10.1002/mrm.20772.
[9] Yen YF, Han KF, Daniel BL, Heiss S, Birdwell RL, Herfkens RJ, et al. Dynamic breast MRI with spiral trajectories: 3D versus 2D. J Magn Reson Imaging 2000;11:351–9.
[10] Haider CR, Hu HH, Campeau NG, Huston III J, Riederer SJ. 3D high temporal and spatial resolution contrast-enhanced MR angiography of the whole brain. Magn Reson Med 2008;60:749–60. http://dx.doi.org/10.1002/mrm.21675.
[11] Lim RP, Shapiro M, Wang EY, Law M, Babb JS, Rueff LE, et al. 3D time-resolved MR angiography (MRA) of the carotid arteries with time-resolved imaging with stochastic trajectories: comparison with 3D contrast-enhanced bolus-chase MRA and 3D time-of-flight MRA. AJNR Am J Neuroradiol 2008;29:1847–54. http://dx.doi.org/10.3174/ajnr.A1252.
[12] Wang K, Busse RF, Holmes JH, Beatty PJ, Brittain JH, Francois CJ, et al. Interleaved variable density sampling with a constrained parallel imaging reconstruction for dynamic contrast-enhanced MR angiography. Magn Reson Med 2011;66:428–36. http://dx.doi.org/10.1002/mrm.22814.
[13] Akçakaya M, Basha TA, Chan RH, Rayatzadeh H, Kissinger KV, Goddu B, et al. Accelerated contrast-enhanced whole-heart coronary MRI using low-dimensional-structure self-learning and thresholding. Magn Reson Med 2012;67:1434–43. http://dx.doi.org/10.1002/mrm.24242.
[14] Saranathan M, Rettmann DW, Hargreaves BA, Clarke SE, Vasanawala SS. Differential subsampling with Cartesian ordering (DISCO): a high spatio-temporal resolution Dixon imaging sequence for multiphasic contrast enhanced abdominal imaging. J Magn Reson Imaging 2012;35:1484–92. http://dx.doi.org/10.1002/jmri.23602.
[15] Lebel RM, Jones J, Ferre J-C, Law M, Nayak KS. Highly accelerated dynamic contrast enhanced imaging. Magn Reson Med 2014;71:635–44. http://dx.doi.org/10.1002/mrm.24710.
[16] Gdaniec N, Eggers H, Börnert P, Doneva M, Mertins A. Robust abdominal imaging with incomplete breath-holds. Magn Reson Med 2014;71:1733–42. http://dx.doi.org/10.1002/mrm.24829.
[17] Du J. Contrast-enhanced MR angiography using time resolved interleaved projection sampling with three-dimensional Cartesian phase and slice encoding

(TRIPPS). Magn Reson Med 2009;61:918–24. http://dx.doi.org/10.1002/mrm.21805.
[18] Prieto C, Uribe S, Razavi R, Atkinson D, Schaeffter T. 3D undersampled golden-radial phase encoding for DCE-MRA using inherently regularized iterative SENSE. Magn Reson Med 2010;64:514–26. http://dx.doi.org/10.1002/mrm.22446.
[19] Doneva M, Stehning C, Nehrke K, Börnert P. Improving scan efficiency of respiratory gated imaging using compressed sensing with 3D Cartesian golden angle sampling. ISMRM 2011:641.
[20] Cheng JY, Uecker M, Alley MT, Vasanawala SS, Pauly JM, Lustig M. Free-breathing pediatric imaging with nonrigid motion correction and parallel imaging. ISMRM 2013:312.
[21] Prieto C, Doneva M, Usman M, Henningsson M, Greil G, Schaeffter T, et al. Highly efficient respiratory motion compensated free-breathing coronary mra using golden-step Cartesian acquisition. J Magn Reson Imaging 2015;41:738–46. http://dx.doi.org/10.1002/jmri.24602.
[22] Pruessmann KP, Weiger M, Scheidegger MB, Boesiger P. SENSE: sensitivity encoding for fast MRI. Magn Reson Med 1999;42:952–62.
[23] Griswold MA, Jakob PM, Heidemann RM, Nittka M, Jellus V, Wang J, et al. Generalized autocalibrating partially parallel acquisitions (GRAPPA). Magn Reson Med 2002;47:1202–10. http://dx.doi.org/10.1002/mrm.10171.
[24] Lustig M, Donoho D, Pauly JM. Sparse MRI: The application of compressed sensing for rapid MR imaging. Magn Reson Med 2007;58:1182–95. http://dx.doi.org/10.1002/mrm.21391.
[25] Nayak KS, Nishimura DG. Randomized trajectories for reduced aliasing artifact. ISMRM 1998;670.
[26] Dippé MAZ, Wold EH. Antialiasing Through Stochastic Sampling. Proc. 12th Annu. Conf. Comput. Graph. Interact. Tech., New York, NY, USA: ACM; 1985. p. 69–78. http://dx.doi.org/10.1145/325334.325182.
[27] Cook RL. Stochastic sampling in computer graphics. ACM Trans Graph 1986;5:51–72. http://dx.doi.org/10.1145/7529.8927.
[28] Mitchell DP. Spectrally Optimal Sampling for Distribution Ray Tracing. Proc. 18th Annu. Conf. Comput. Graph. Interact. Tech., New York, NY, USA: ACM; 1991. p. 157–64. http://dx.doi.org/10.1145/122718.122736.
[29] Dunbar D, Humphreys G. A Spatial Data Structure for Fast Poisson-disk Sample Generation. ACM SIGGRAPH 2006 Pap. New York, NY, USA: ACM; 2006. p. 503–8. http://dx.doi.org/10.1145/1179352.1141915.
[30] Bridson R. Fast Poisson Disk Sampling in Arbitrary Dimensions. ACM SIGGRAPH 2007 Sketches. New York, NY, USA: ACM; 2007. http://dx.doi.org/10.1145/1278780.1278807.
[31] Zhu Y, Guo Y, Lebel RM, Law M, Nayak KS. Randomized golden ratio sampling for highly accelerated dynamic imaging. ISMRM 2014;4365.
[32] Winkelmann S, Schaeffter T, Koehler T, Eggers H, Doessel O. An optimal radial profile order based on the golden ratio for time-resolved MRI. IEEE Trans Med Imaging 2007;26:68–76. http://dx.doi.org/10.1109/TMI.2006.885337.
[33] Liu B, Zou YM, Ying L. Sparsesense: Application of compressed sensing in parallel MRI. Int. Conf. Inf. Technol. Appl. Biomed. 2008 ITAB 2008; 2008. p. 127–30. http://dx.doi.org/10.1109/ITAB.2008.4570588.
[34] King KF. Combining compressed sensing and parallel imaging. ISMRM 2008:1488.
[35] Ramirez-Giraldo JC, Trzasko J, Leng S, Yu L, Manduca A, McCollough CH. Nonconvex prior image constrained compressed sensing (NCPICCS): theory and simulations on perfusion CT. Med Phys 2011;38:2157–67.
[36] Sourbron SP, Buckley DL. On the scope and interpretation of the tofts models for DCE-MRI. Magn Reson Med 2011;66:735–45. http://dx.doi.org/10.1002/mrm.22861.
[37] Tofts P. T1-weighted DCE imaging concepts: modelling. Acquisition and Analysis Signal, 500. ; 2010. p. 400.
[38] Parker GJM, Roberts C, Macdonald A, Buonaccorsi GA, Cheung S, Buckley DL, et al. Experimentally-derived functional form for a population-averaged high-temporal-resolution arterial input function for dynamic contrast-enhanced MRI. Magn Reson Med 2006;56:993–1000. http://dx.doi.org/10.1002/mrm.21066.
[39] Deoni SCL. High-resolution T1 mapping of the brain at 3 T with driven equilibrium single pulse observation of T1 with high-speed incorporation of RF field inhomogeneities (DESPOT1-HIFI). J Magn Reson Imaging 2007;26:1106–11. http://dx.doi.org/10.1002/jmri.21130.
[40] Tofts PS, Kermode AG. Measurement of the blood–brain barrier permeability and leakage space using dynamic MR imaging. 1. Fundamental concepts. Magn Reson Med 1991;17:357–67.
[41] Adcock B, Hansen AC, Poon C, Roman B. Breaking the coherence barrier: a new theory for compressed sensing. ArXiv E-Prints 2013;1302:561.
[42] Lingala SG, Hu Y, DiBella E, Jacob M. Accelerated dynamic MRI exploiting sparsity and low-rank structure: k-t SLR. IEEE Trans Med Imaging 2011;30:1042–54. http://dx.doi.org/10.1109/TMI.2010.2100850.
[43] Lingala SG, Jacob M. Blind compressive sensing dynamic MRI. IEEE Trans Med Imaging 2013;32:1132–45. http://dx.doi.org/10.1109/TMI.2013.2255133.